Solar Radiative Transfer in Cirrus Clouds. Part I: Single-Scattering and Optical Properties of Hexagonal Ice Crystals

YOSHIHIDE TAKANO AND KUO-NAN LIOU

Department of Meteorology, University of Utah, Salt Lake City, Utah

(Manuscript received 1 February 1988, in final form 13 June 1988)

ABSTRACT

We have developed an efficient light scattering and polarization program, based on a ray-tracing technique, for hexagonal ice crystals randomly and horizontally oriented in space. Improvements have been made on the ray-tracing computations through a proper treatment of the δ-forward transmission by geometric rays and incorporation of the effects of birefringence of ice. Using this program, computations of the scattering phase matrix are made from the observed ice crystal size distributions for four typical cirrus clouds. The results for single-scattering parameters, including the phase function, single-scattering albedo, extinction cross section, and asymmetry factor for five solar wavelengths, are presented and discussed. Moreover, we show that the assumption of equivalent spheres with the same surface areas as hexagonal ice crystals leads to larger asymmetry factors for all wavelengths and smaller single-scattering albedos for near IR wavelengths. The computed phase matrix elements compare reasonably well with experimental scattering results for laboratory ice crystal clouds. In particular, we illustrate that the neutral point (angle of zero linear polarization) is sensitive to the ice crystal shape. Thus, an observation of this position from space could provide a means for determining the aspect ratio of cloud particles. Light scattering computations are also made for horizontally oriented columns and plates of various sizes. Results are used to interpret the optical phenomena produced by cirrus clouds. The present light scattering program for hexagonal columns and plates identifies the positions of halos and arcs, as well as providing relative intensities for these optical features.

1. Introduction

Cirrus clouds have been identified as one of the major unsolved elements in weather and climate research (Liou 1986). There are significant problems in the development of satellite remote sensing techniques for the mapping of cirrus clouds due to their nonblackness, high altitude, and nonspherical ice crystals. Recently, intensive field observations of cirrus clouds have been conducted as a major component of the First ISCCP Regional Experiment (Starr 1987) to assist in the development of remote sensing methodologies for the determination of the temperature and optical properties of cirrus clouds. Moreover, the manner in which the formation of cirrus clouds and coupled radiative properties may be properly and effectively incorporated in large-scale numerical models is a subject unlikely to be resolved without considerable research effort.

To be successful in the development of retrieval methodologies for the detection of cirrus clouds, and parameterizations for their radiative properties for incorporation in dynamic models, we must have fundamental scattering and absorption data for nonspherical ice crystals that are appropriate for cirrus clouds. From in situ aircraft observations, it has been determined that cirrus clouds are largely composed of nonspherical bullets, columns, and plates (see, e.g., Heymsfield and Platt 1984). For radiative transfer calculations, nonspherical ice crystals have been approximated by spherical particles (see, e.g., Plass and Kattawar 1968). Liou (1972) made the first attempt to model the single-scattering properties of nonspherical ice crystals using the scattering solution for long circular cylinders. Stephens (1980) adopted this cylindrical scattering solution to perform light scattering and radiative transfer calculations for ice clouds. Welch et al. (1980) derived the radiative properties of ice clouds using a semiempirical approach through a modification of the Mie solution for spherical particles. Although the aforementioned models can represent some aspects of the scattering and radiative characteristics of cirrus clouds, none of these approaches account for the hexagonal structure of ice crystals. Optical phenomena, such as halos and numerous arcs associated with cirrus, cannot be reproduced from scattering solutions for circular cylinders and spheres. Rainbows produced by spherical droplets are absent in cirrus. Moreover, the specific scattering and absorption features associated with the hexagonal structure, aspect ratio (length/diameter), and orientation of ice crystals could be important in the determination of bidirectional reflec-

Corresponding author address: Dr. Kuo-Nan Liou, Dept. of Meteorology, 819 Wm. C. Browning Building, University of Utah, Salt Lake City, UT 84112.

tance, cloud albedo and transmittance, sky polarization configurations, and atmospheric heating rates.

In recent years, light scattering and absorption programs for hexagonal columns and plates have been developed by Cai and Liou (1982) and Takano and Jayaweera (1985) based on a ray-tracing technique. In this paper, we have extended these programs by taking into account the ice crystal size distribution, as well as the possibility of horizontal orientation. In addition, improvements have been made on the light scattering program by proper summation of contributions due to geometric reflection and refraction and Fraunhofer diffraction, and by incorporation of the birefringence properties of ice. We shall demonstrate that the present scattering program for hexagonal particles is appropriate for modeling the scattering characteristics of ice crystal clouds. This is done by comparing the computed and measured scattering and polarization patterns, as well as by interpreting the observed optical features produced by cirrus clouds.

In section 2, we present single-scattering properties for randomly oriented hexagonal ice crystals. The computed scattering and polarization results are then compared with available measurement data in section 3. In section 4 we report single-scattering properties for horizontally oriented columns and plates and provide explanations for numerous halos and arcs that have been observed in the atmosphere. Finally, conclusions are given in section 5.

2. Single-scattering properties of randomly oriented hexagonal ice crystals

The basic formulation for the computation of reflection, refraction, and diffraction of light rays in the limit of geometric optics has been presented in our previous papers (Cai and Liou 1982; Takano and Jayaweera 1985). Thus, we shall briefly describe improvements and refinements that have been made in the current light scattering program, which are pertinent to the presentation of scattering and absorption results for oriented hexagonal ice crystals.

Ice is a uniaxial, doubly refracting, and optically positive crystal. The refracted rays split into ordinary and extraordinary components. The vibrational planes of the electric field vectors of these two rays are orthogonal to each other. This phenomenon is referred to as birefringence. Its effect on polarization and intensity distributions of halos has been investigated by Können (1983). We shall briefly discuss the manner in which this effect is incorporated in the present ray-tracing program.

According to Born and Wolf (1975), the effective index of refraction for extraordinary rays, n_{eff}, is given by

$$\frac{1}{n_{\text{eff}}^2} = \frac{\cos^2\kappa}{n_o^2} + \frac{\sin^2\kappa}{n_e^2}, \tag{1}$$

where n_o and n_e are, respectively, the indices of refraction for ordinary and extraordinary rays, and κ is the angle between the optical axis (c-axis) of the crystal and the light ray in the crystal, as shown in Fig. 1. The optical path lengths for ordinary rays, δ_o and extraordinary rays, δ_e may be expressed, respectively, by

$$\left.\begin{aligned} \delta_o^k &= -\frac{2\pi}{\lambda} n_o d_{k+1,k} \\ \delta_e^k &= -\frac{2\pi}{\lambda} n_{\text{eff}} d_{k+1,k} \end{aligned}\right\}, \quad k \geq 1 \tag{2}$$

where λ is the wavelength of the incident light and $d_{k+1,k}$ is the path length between points N_k and N_{k+1}, defined in Fig. 1.

To incorporate the effects of birefringence, the amplitude matrix, which is related to the electric field, requires modifications. After each refraction or reflection, the coordinate axis is rotated by an appropriate angle so that the reference plane for polarization coincides with the plane including the light ray and c-axis. The amplitudes of the extraordinary and ordinary rays are then multipled, respectively, by the factors $e^{i\delta e}$ and $e^{i\delta o}$. The coordinate axis is subsequently rotated back to the original plane.

In the limit of geometric optics, half of the incident energy is associated with the diffracted rays. However, in the process of normalizing the phase function by numerical means, the 0° forward (hereafter referred to as the δ-function) transmission by two direct 0° refractions through parallel planes (e.g., a basal plane and opposite basal plane) cannot be properly accounted for. This δ-function transmission component, which differs from diffracted rays, is important for both absorption and nonabsorption cases. In the Appendix we describe a procedure by which the addition of geometric and diffracted rays and the associated normalization for the phase function may be performed correctly.

For randomly oriented ice crystals, integration of the phase matrix over all possible orientations must be carried out so that

$$\hat{P}_{kl}(\Theta) = \frac{6}{\pi}\int_0^{\pi/6}\int_0^{\pi/2} G_{kl}(\alpha, \beta, \Theta)\cos\alpha d\alpha d\beta, \quad k, l = 1\text{–}4 \tag{3}$$

where Θ denotes the scattering angle, α is the complementary angle between the incident ray and c axis, β the rotational angle about the c axis (see Fig. 1), and G_{kl} represents four-by-four phase matrix elements for a single crystal. Because of the symmetry of the hexagonal crystal, integration of the angle β is from 0 to $\pi/6$. The scattering cross section for randomly oriented ice crystals is given by

$$\hat{C}_s = \frac{6}{\pi}\int_0^{\pi/6}\int_0^{\pi/2} \hat{C}_s(\alpha, \beta)\cos\alpha d\alpha d\beta, \tag{4}$$

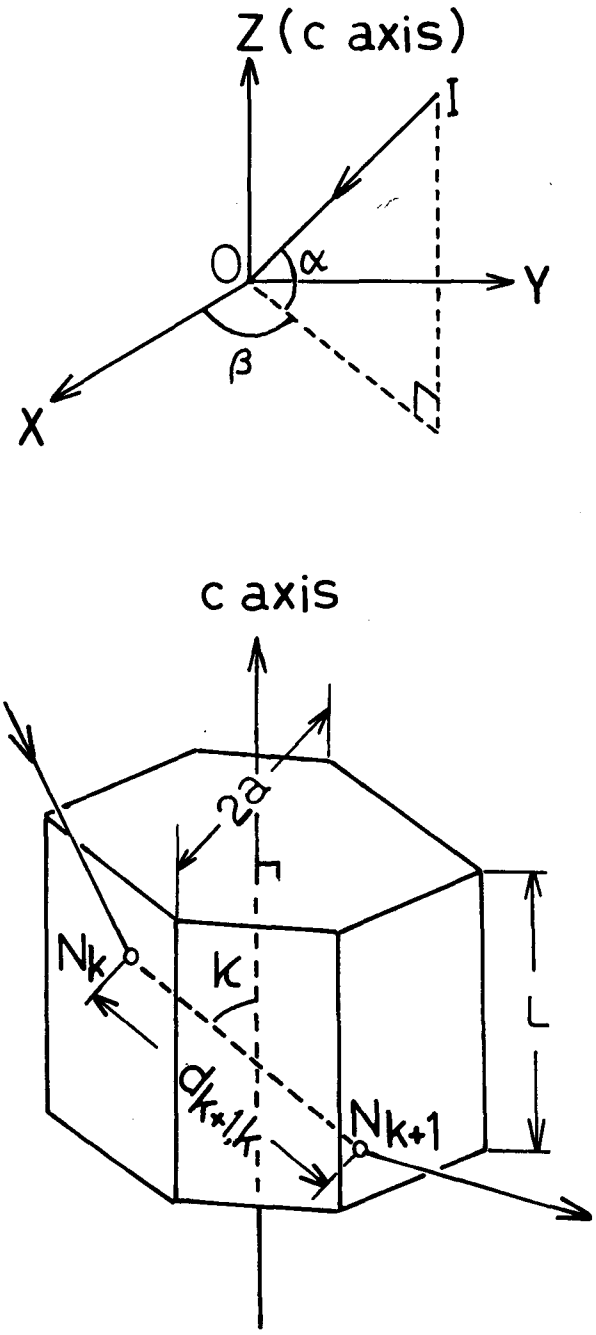

FIG. 1. Geometry of a light ray in an ice crystal. All symbols are explained in the text.

where the scattering cross section for a single crystal $\hat{C}_s(\alpha, \beta)$ is computed by integration of the phase matrix element G_{11} over the 4π solid angle (van de Hulst 1957). According to the optical theorem, the extinction cross section of a single particle is twice the geometric cross section area in the limit of geometric optics. For an arbitrarily oriented hexagon, the geometric cross section area σ is

$$\sigma(\alpha, \beta) = \frac{3\sqrt{3}}{2} a^2 \sin\alpha + 2aL \cos\alpha \cos\left(\frac{\pi}{6} - \beta\right), \quad (5)$$

where L is the length of the hexagon and a the radius. Thus, the extinction cross section for a sample of randomly oriented ice crystals with the same sizes may be expressed in the form

$$\hat{C}_e = \frac{6}{\pi} \int_0^{\pi/6} \int_0^{\pi/2} 2\sigma(\alpha, \beta) \cos\alpha d\alpha d\beta$$

$$= \frac{3a^2}{2} [\sqrt{3} + 4(L/2a)] = A/2, \quad (6)$$

where A is the surface area of a hexagonal cylinder. The last expression was pointed out by Vouk (1948) for randomly oriented convex particles.

Next, we shall discuss the manner in which the ice crystal size distribution is incorporated in the computation of the single-scattering parameters. Based on observations by Ono (1969) and Auer and Veal (1970), the aspect ratio, $L/2a$, of ice crystals may be related to the crystal length L. If the ice crystal size distribution is denoted by $n(L)$, then the phase matrix for a sample of ice crystals of different sizes may be obtained from

$$P_{kl}(\Theta) = \frac{\int_{L_1}^{L_2} \hat{P}_{kl}(\Theta, L) \hat{C}_s(L) n(L) dL}{\int_{L_1}^{L_2} \hat{C}_s(L) n(L) dL}, \quad (7)$$

where L_1 and L_2 are the lower and upper limits of crystal lengths. The scattering and extinction cross sections for a sample of ice crystals of different sizes are then given by

$$C_{s,e} = \frac{1}{N_o} \int_{L_1}^{L_2} \hat{C}_{s,e}(L) n(L) dL, \quad (8)$$

where

$$N_o = \int_{L_1}^{L_2} n(L) dL,$$

the total number of ice crystals. The single-scattering albedo is defined by

$$\tilde{\omega} = C_s / C_e. \quad (9)$$

In the present computations, four ice crystal size distributions were used. The first two are for the cirrostratus (Cs) and cirrus uncinus (Ci) presented by Heymsfield (1975), while the other two are modified distributions given by Heymsfield and Platt (1984) corresponding to warm and cold cirrus clouds. These size distributions are displayed in Fig. 2. For scattering calculations, we have discretized these size distributions in five regions, as shown in Fig. 2. The aspect ratios, $L/2a$, used are 20/20, 50/40, 120/60, 300/100, and 750/160 in units of micrometers/micrometers, roughly

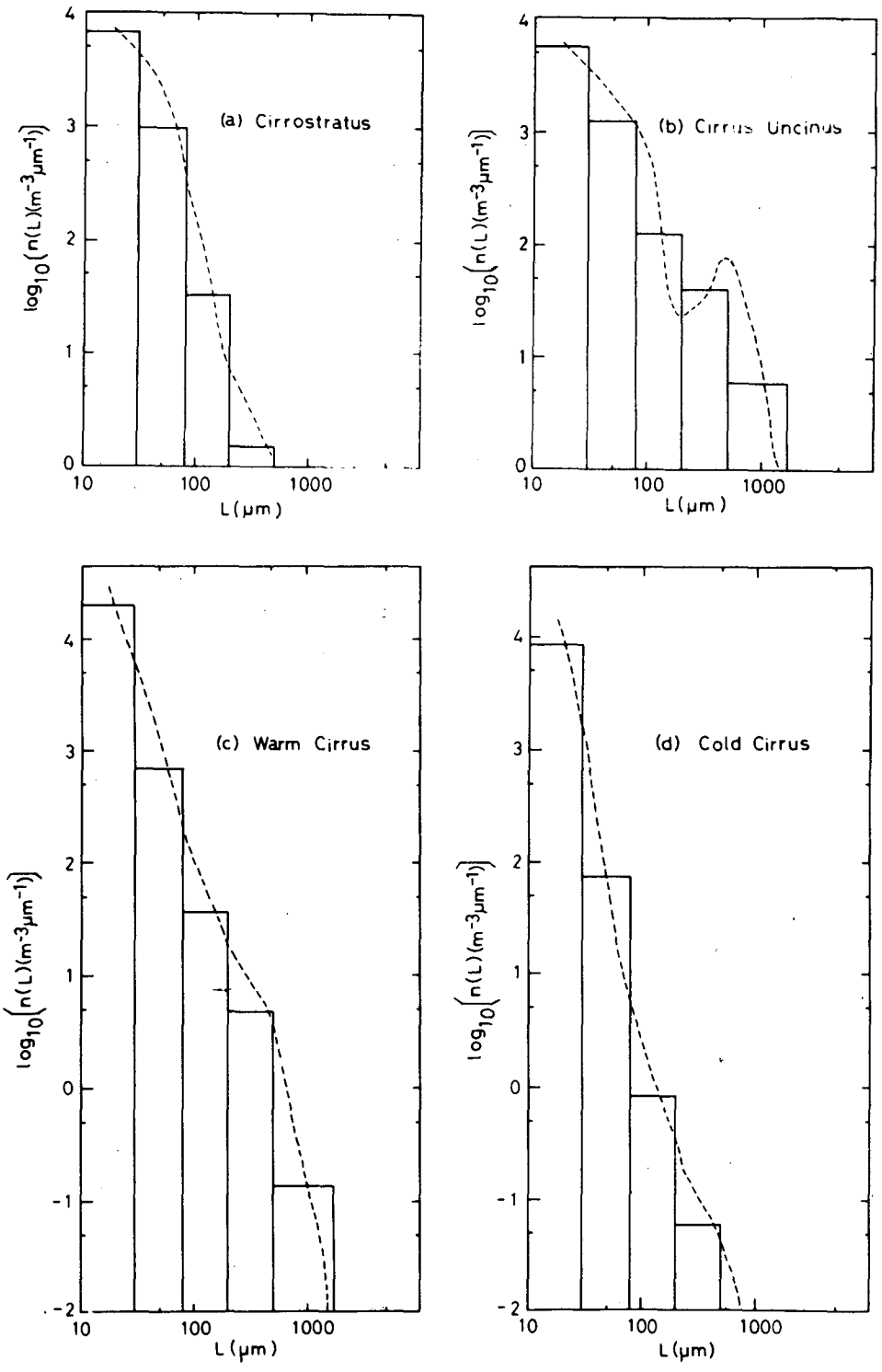

FIG. 2. Measured cirrus cloud particle size distributions (dashed lines) and the discretized size distributions (vertical bars) for (a) cirrostratus, (b) cirrus uncinus, (c) warm cirrus, and (d) cold cirrus.

corresponding to the observations reported by Ono (1969) and Auer and Veal (1970). The relationships between the crystal length L and diameter $2a$ derived by these researchers may not be universal, but these are the best experimental results that are available at the present time. The refractive indices for ice compiled by Warren (1984) were used in the scattering calculations.

Figure 3 shows the phase function as a function of the scattering angle for Cs and Ci at the 0.55 μm wavelength. In the numerical computations, we find that the intervals for orientation angles $\Delta\beta = 0.5°$ and $\Delta\alpha = 1°$ are sufficient to produce a smooth phase function curve. For the warm and cold Ci presented in Fig. 2, the phase functions are close to those for Cs and are not presented in the diagram. The 22° and 46° halos produced by two refracted rays are well illustrated in the diagram, in addition to the forward diffraction peak. For scattering angles between about 150° and 160°, there is also a maximum produced by rays undergoing two internal reflections. Table 1 lists the visible phase function values as a function of the scattering angle for Cs. From 0° to 2°, the values are given for every 0.1°, otherwise they are listed for every 1°. This table should be of use to researchers who are interested in investigating the effect of nonsphericity on the transfer of solar radiation, as well as developing an independent light scattering program for hexagonal ice crystals.

In Table 2 are shown the extinction coefficient $\beta_e = N_o C_e$, single-scattering albedo $\tilde{\omega}$, and asymmetry factor defined by

$$g = \frac{1}{2}\int_{-1}^{1} P_{11}(\Theta)\cos\Theta d\cos\Theta, \qquad (10)$$

for the four ice crystal size distributions shown in Fig. 2 and for five wavelengths in the solar spectrum. Cirrus (uncinus) contains a significant amount of large ice crystals in the second peak of the size distribution, as shown in Fig. 2. For this reason, the extinction coefficient β_e for this cloud is much larger than those for the three other cloud types. In connection with the discussion in the Appendix, when the asymmetry factor is calculated from the phase function values listed in Table 1, the contribution from the δ-function transmission f_δ ($\Theta = 0°$) cannot be accounted for numerically. Using the similarity principle, the correct asymmetry factor may be expressed by $g = (1 - f_\delta)g^* + f_\delta$, where g^* represents the asymmetry factor without incorporation of the δ-function transmission. In the present case, $g^* = 0.751$ and $f_\delta = 0.126$. The correct g, including the contribution of f_δ denoted in Fig. A1 in the Appendix, is 0.782. The complex indices of refraction at each wavelength are averaged values over the wavelength band listed in the table, weighted by the solar irradiance (Thekaekara 1973). The extinction coefficients β_e in the limit of geometric optics for a given size distribution are the same regardless of the wavelength. The optical depth $\tau = \beta_e \Delta z$, corresponding to each size distribution, can be obtained if the cloud thickness Δz is given. There is significant absorption at the 3.0 μm wavelength with single-scattering albedos of about 0.53 that are almost independent of the size distribution. Considerable absorption is noted for the 1.6 and 2.2 μm wavelengths for cirrus uncinus consisting of large ice crystal sizes. At a given wavelength, the asymmetry factors for Cs, Ci (warm), and Ci (cold) are about the same since the phase functions for these clouds are very similar. For a given size distribution, the asymmetry factor increases toward the longer wavelength, where absorption is increased, leading to sharper diffraction patterns. The values listed in the table should be of use for applications to the calculation of the radiative transfer of cirrus clouds covering the solar spectrum.

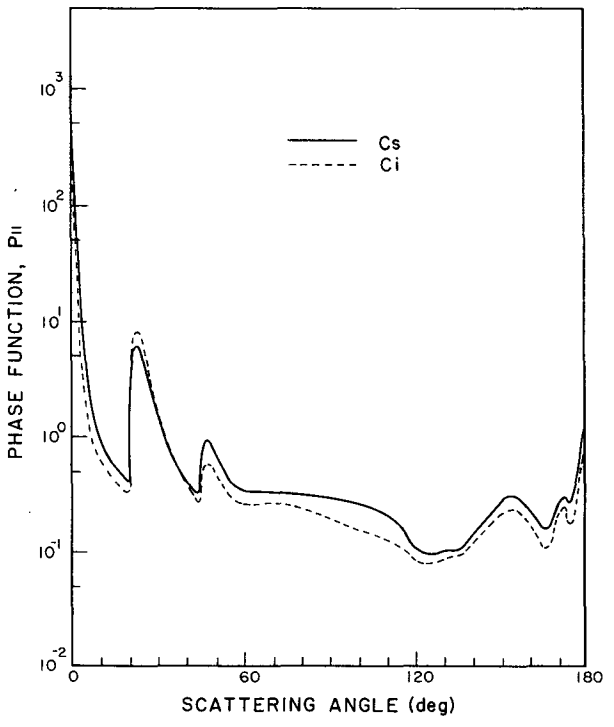

FIG. 3. Phase functions as a function of the scattering angle for cirrostratus and cirrus uncinus at the 0.55 μm wavelength.

As shown in Warren (1984), the imaginary part m_i of the refractive index for ice varies about six orders of magnitude in the near infrared region. Moreover, m_i is uncertain to about a factor of 2 in the near infrared. We wish to develop a parameterization equation to relate the single-scattering albedo $\tilde{\omega}$ to the absorption coefficient $k_i = 4\pi m_i/\lambda$ and aspect ratio $L/2a$. We note that $1 - \tilde{\omega} = C_a/C_e$, where C_a and C_e denote the absorption and extinction cross sections, respectively. The absorption cross section, C_a, is proportional to the product of the absorption coefficient and volume, i.e., $C_a \sim k_i V$ when the absorption is small, and C_e is given in Eq. (6). For a hexagonal cylinder, $V = 3\sqrt{3}a^2(L/2a)$. Thus, C_a/C_e must be proportional to the physical parameter defined by

$$z = k_i a \frac{3\sqrt{3}(L/2a)}{\sqrt{3} + 4(L/2a)}. \qquad (11)$$

Using 60 values of $k_i a$ and $L/2a$, computations of the single-scattering albedo were performed for a number of ice crystal sizes. We then performed a least squares fit to obtain the following parameterized equation:

TABLE 1. Scattering phase function for the cirrostratus cloud model at $\lambda = 0.55$ μm.

Θ	P_{11}	Θ	P_{11}	Θ	P_{11}	Θ	P_{11}
.00	1.083 +05*	32	1.13 +00	82	3.18 −01	132	1.04 −01
.10	6.037 +04	33	9.85 −01	83	3.14 −01	133	1.02 −01
.20	3.231 +04	34	8.54 −01	84	3.11 −01	134	1.02 −01
.30	1.809 +04	35	7.24 −01	85	3.11 −01	135	9.96 −02
.40	9.985 +03	36	6.26 −01	86	3.08 −01	136	1.02 −01
.50	5.477 +03	37	5.55 −01	87	3.03 −01	137	1.12 −01
.60	3.210 +03	38	5.55 −01	88	2.98 −01	138	1.21 −01
.70	2.106 +03	39	4.45 −01	89	2.95 −01	139	1.27 −01
.80	1.502 +03	40	4.12 −01	90	2.91 −01	140	1.35 −01
.90	1.095 +03	41	4.03 −01	91	2.89 −01	141	1.44 −01
1.00	7.875 +02	42	3.74 −01	92	2.87 −01	142	1.54 −01
1.10	5.550 +02	43	3.57 −01	93	2.85 −01	143	1.66 −01
1.20	3.885 +02	44	4.09 −01	94	2.83 −01	144	1.78 −01
1.30	2.758 +02	45	5.44 −01	95	2.82 −01	145	1.91 −01
1.40	2.027 +02	46	7.44 −01	96	2.81 −01	146	2.04 −01
1.50	1.563 +02	47	8.88 −01	97	2.78 −01	147	2.13 −01
1.60	1.267 +02	48	8.78 −01	98	2.75 −01	148	2.25 −01
1.70	1.069 +02	49	8.10 −01	99	2.72 −01	149	2.43 −01
1.80	9.266 +01	50	7.15 −01	100	2.68 −01	150	2.63 −01
1.90	8.151 +01	51	6.56 −01	101	2.62 −01	151	2.87 −01
2.00	7.210 +01	52	5.91 −01	102	2.56 −01	152	3.04 −01
3.00	2.223 +01	53	5.09 −01	103	2.53 −01	153	3.08 −01
4.00	9.666 +00	54	4.52 −01	104	2.48 −01	154	3.09 −01
5.00	5.198 +00	55	4.16 −01	105	2.42 −01	155	3.07 −01
6.00	3.208 +00	56	3.89 −01	106	2.35 −01	156	2.99 −01
7.00	2.182 +00	57	3.72 −01	107	2.27 −01	157	2.80 −01
8.00	1.598 +00	58	3.58 −01	108	2.21 −01	158	2.63 −01
9.00	1.236 +00	59	3.47 −01	109	2.16 −01	159	2.52 −01
10.00	1.013 +00	60	3.46 −01	110	2.11 −01	160	2.36 −01
11.00	8.296 −01	61	3.44 −01	111	2.05 −01	161	2.13 −01
12.00	7.494 −01	62	3.43 −01	112	1.99 −01	162	1.95 −01
13.00	6.753 −01	63	3.44 −01	113	1.96 −01	163	1.77 −01
14.00	6.220 −01	64	3.43 −01	114	1.89 −01	164	1.66 −01
15.00	5.681 −01	65	3.40 −01	115	1.79 −01	165	1.57 −01
16.00	5.248 −01	66	3.38 −01	116	1.64 −01	166	1.58 −01
17.00	4.883 −01	67	3.37 −01	117	1.42 −01	167	1.69 −01
18.00	4.598 −01	68	3.36 −01	118	1.27 −01	168	1.90 −01
19.00	4.409 −01	69	3.36 −01	119	1.18 −01	169	2.35 −01
20.00	4.227 −01	70	3.36 −01	120	1.11 −01	170	2.71 −01
21.00	1.935 +00	71	3.35 −01	121	1.04 −01	171	2.84 −01
22.00	5.333 +00	72	3.34 −01	122	9.93 −02	172	2.88 −01
23.00	6.137 +00	73	3.33 −01	123	9.86 −02	173	2.63 −01
24.00	6.043 +00	74	3.32 −01	124	9.79 −02	174	2.67 −01
25.00	4.660 +00	75	3.31 −01	125	9.70 −02	175	3.04 −01
26.00	3.665 +00	76	3.29 −01	126	9.67 −02	176	3.81 −01
27.00	2.955 +00	77	3.27 −01	127	9.68 −02	177	5.76 −01
28.00	2.404 +00	78	3.25 −01	128	9.76 −02	178	7.98 −01
29.00	1.982 +00	79	3.24 −01	129	9.97 −02	179	1.01 +00
30.00	1.638 +00	80	3.22 −01	130	1.01 −01	180	1.18 +00
31.00	1.342 +00	81	3.21 −01	131	1.03 −01		

* 1.083 +05 means 1.083×10^5.

$$\tilde{\omega} = 1 - b_1 z + b_2 z^2 - b_3 z^3 + b_4 z^4, \qquad (12)$$

where the empirical coefficients $b_1 = 1.1128$, $b_2 = 2.5576$, $b_3 = 5.6257$, and $b_4 = 5.9498$. Equation (12) is applicable for $\tilde{\omega}$ in the range from 0.75 to 1. It follows that if m_i is given, $\tilde{\omega}$ can be determined for a given size and wavelength. Equation (11) is valid for $0.4 \leqslant \lambda \leqslant 2.5$ μm.

Next, we investigate the effects of nonsphericity on the single-scattering parameters using two wavelengths of 0.55 (negligible absorption) and 2.2 μm (moderate absorption), and the five hexagonal particle sizes listed in Table 3. The single-scattering properties for equivalent ice spheres with the same surface areas as those for hexagons were computed by the Mie theory. The asymmetry factors for hexagonal ice crystals are uniformly smaller than those for equivalent ice spheres. This is especially evident for small sizes illuminated by visible light. The single-scattering co-albedos $1 - \tilde{\omega}$ for hexagonal ice crystals at 2.2 μm are smaller than those for equivalent ice spheres. The differences are especially evident for large particles. This is partly due to the fact that equivalent ice spheres have larger volumes and hence, absorb more incident radiation. For the extinc-

TABLE 2. Extinction coefficient β_e (km^{-1}),* single-scattering albedo $\tilde{\omega}$, and asymmetry factor g for four cirrus models and five solar wavelengths. The refractive index $m = m_r - im_i$, where m_r and m_i are averaged real and imaginary parts for the spectral band with limits λ_1 and λ_2.

λ (μm) (λ_1, λ_2)	m_r	m_i		Cs	Ci uncinus	Ci (warm)	Ci (cold)
			β_e	0.3865	2.6058	0.6525	0.1662
0.55	1.311	3.110 −9**	$\tilde{\omega}$	1.0000†	1.0000†	1.0000†	1.0000†
			g	0.7824	0.8404	0.7889	0.7724
			β_e	0.3865	2.6058	0.6525	0.1662
1.0	1.302	1.931 −6	$\tilde{\omega}$	0.9995	0.9981	0.9994	0.9997
(0.7, 1.3)			g	0.7905	0.8448	0.7945	0.7780
			β_e	0.3865	2.6058	0.6525	0.1662
1.6	1.290	2.128 −4	$\tilde{\omega}$	0.9658	0.9004	0.9628	0.9810
(1.3, 1.9)			g	0.8100	0.8778	0.8129	0.7925
			β_e	0.3865	2.6058	0.6525	0.1662
2.2	1.263	7.997 −4	$\tilde{\omega}$	0.9185	0.7996	0.9154	0.9528
(1.9, 2.5)			g	0.8436	0.9116	0.8440	0.8220
			β_e	0.3865	2.6058	0.6525	0.1662
3.0	1.242	1.424 −1	$\tilde{\omega}$	0.5321	0.5309	0.5327	0.5338
(2.5, 3.5)			g	0.9653	0.9728	0.9634	0.9583

* The number densities N_0 for Cs, Ci, Ci (warm), and Ci (cold) are 0.187, 0.213, 0.442, and 0.176 cm^{-3}, respectively.
** 3.110 −9 means 3.110×10^{-9}.
† $\tilde{\omega} = 0.99999$.

tion cross section at 0.55 μm, the results for randomly oriented hexagons computed from geometric optics are very close to those for equivalent spheres with the same surface areas. Note that in the limit of geometric optics, the extinction is independent of the wavelength. We also performed light scattering calculations using equivalent ice spheres with the same volumes as hexagons. The results show that the single-scattering albedos for equivalent volume spheres are closer to those for hexagons, but the extinction cross sections are smaller. The latter will lead to a smaller optical depth if spheres and hexagons have the same number density in a cloud. On the basis of the preceding comparisons, we conclude that neither the area-equivalent nor the volume-equivalent ice sphere can adequately approximate nonspherical ice crystals in terms of their scattering and absorption properties. This conclusion agrees with the criticism of using an "equivalent sphere" for nonspherical particles presented by Bohren (1986).

3. Comparisons with measurements

In this section, the computed phase matrix elements for hexagonal ice crystals are compared with experimental results. Dugin and Mirumyants (1976) measured the phase matrix elements for laboratory ice clouds containing 20–100 μm plates at the 0.57 μm wavelength. The ice crystals generated in the cold chamber were smaller than those occurring in cirrus

TABLE 3. Extinction cross section, single-scattering albedo, and asymmetry factor for hexagonal ice crystals and area equivalent ice spheres at $\lambda = 0.55$ and 2.2 μm.

$L/2a$		C_e (cm^2)		$1 - \tilde{\omega}$		g	
(μm/μm)	λ (μm)	Hexagon	Sphere	Hexagon	Sphere	Hexagon	Sphere
20/20	0.55	8.598 −6*	8.918 −6	0	0	0.7704	0.8759
	2.2	8.598 −6	9.441 −6	4.085 −2	4.944 −2	0.8185	0.8729
50/40	0.55	4.039 −5	4.129 −5	0	0	0.7780	0.8837
	2.2	4.039 −5	4.270 −5	8.179 −2	9.550 −2	0.8416	0.8996
120/60	0.55	1.314 −4	1.334 −4	0	0	0.8155	0.8871
	2.2	1.314 −4	1.364 −4	1.246 −1	1.539 −1	0.8829	0.9174
300/100	0.55	5.150 −4	5.198 −4	0	0	0.8429	0.8895
	2.2	5.150 −4	5.273 −4	1.871 −1	2.504 −1	0.9165	0.9373
750/160	0.55	1.966 −3	1.978 −3	0	0	0.8592	0.8908
	2.2	1.966 −3	1.996 −3	2.503 −1	3.583 −1	0.9380	0.9566

* 8.598 −6 means 8.598×10^{-6}.

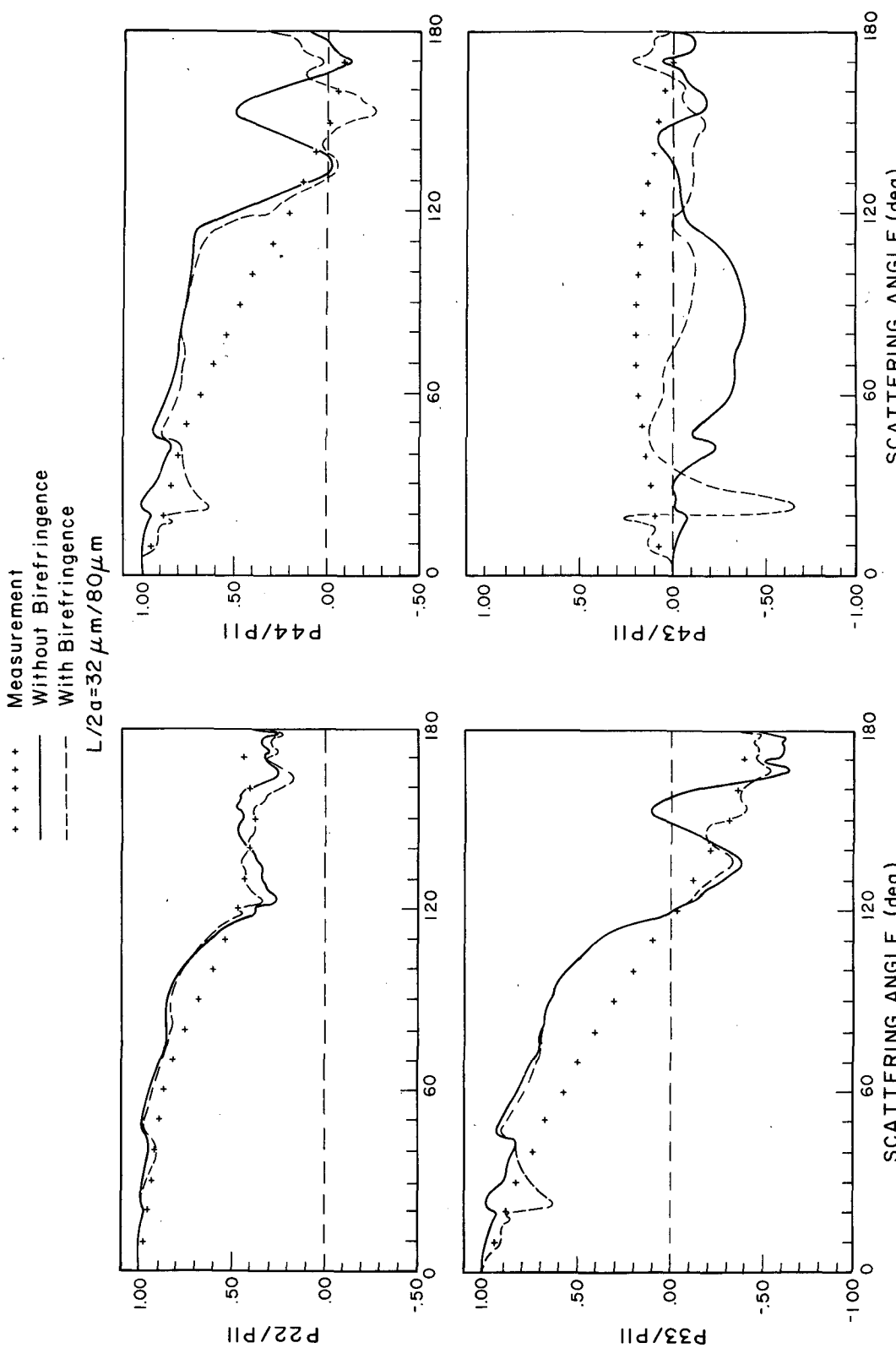

FIG. 4. Scattering phase matrix elements for randomly oriented hexagonal plate crystals with an aspect ratio $L/2a$ of 32 μm/80 μm at the 0.55 μm wavelength. The birefringence, $n_e - n_o$, is 0.0014. The plus symbols are experimental values reported by Dugin and Mirumyants (1976).

clouds. Small ice crystals tend to be randomly oriented (Fraser 1979). For randomly oriented nonspherical particles, the phase matrix consists of only six nonzero and independent elements in the form

$$\mathbf{P} = \begin{bmatrix} P_{11} & P_{12} & 0 & 0 \\ P_{12} & P_{22} & 0 & 0 \\ 0 & 0 & P_{33} & -P_{43} \\ 0 & 0 & P_{43} & P_{44} \end{bmatrix}. \quad (13)$$

The laboratory data were normalized by the phase function P_{11}.

We first compare the computed and measured elements P_{22}/P_{11}, P_{33}/P_{11}, P_{43}/P_{11}, and P_{44}/P_{11}. A number of mean aspect ratios were used to interpret the observed data. We find that $L/2a$ of 32 μm/80 μm, as well as 8 μm/80 μm, closely match the measurements. Note that incorporation of the birefringence effect requires size information. The theoretical results with and without the effect of birefringence, along with the measured data are shown in Fig. 4. The effect of birefringence on the phase function and degree of linear polarization is insignificant, although this effect somewhat modifies the other phase matrix elements. The computed phase matrix element P_{22}/P_{11} agrees well with the measured value. Except for the element P_{43}/P_{11}, the incorporation of the birefringence effect brings the computed values closer to the measured values, especially in the scattering angle range between 140° and 160°. An agreement can be seen between the computed and measured values at the scattering angle Θ_{33} where the element P_{33} becomes zero. Table 4 lists Θ_{33} for several aspect ratios $L/2a$. Based on the laboratory experiment for plate crystals, $\Theta_{33} = 117°$, as shown in Fig. 4. The computed Θ_{33} for the aspect ratio of 32 μm/80 μm is about 120°, which agrees well with the experimental value. The scattering angle Θ_{33} varies with the aspect ratio and shows a maximum value when the length and width are about the same ($L/2a = 0.8$). Similar behaviors for needles and circular plates have been reported by Asano and Sato (1980) in light scattering calculations using spheroidal shapes. They showed that the Θ_{33} value for spheroids with an aspect ratio of 2 is larger than that with a larger aspect ratio of 5.

The computed values of P_{43}/P_{11} are also in general agreement with the measured values if the sign of P_{43} from the laboratory experiments is reversed. It appears that the sign of P_{43} is defined differently by Dugin and Mirumyants. This is likely a case where different conventions for right- and left-circular polarization are used. At the 22° scattering angle, there is a significant difference between the computed P_{43}/P_{11} values with and without the incorporation of the birefringence effect. This behavior can be explained as follows. The inner halo rays that undergo two refractions produce a maximum intensity at the 22° scattering angle. When the effect of birefringence is not considered, the element P_{43} basically arises from total reflection and has positive values. When the birefringence effect is accounted for in the computation, the optical path length due to extraordinary rays δ_e is smaller than that due to ordinary rays δ_o. Since the element P_{43} for two refracted rays is proportional to $\sin(\delta_e - \delta_o)$, its value at the inner halo angle becomes negative.

TABLE 4. Scattering angle Θ_{33} where P_{33} becomes zero.

$L/2a$ (μm/μm)	Θ_{33} (°) Without birefringence	Θ_{33} (°) With birefringence
8/80	114.0 (99.7)*	115.0
16/80	116.1	116.4
32/80	119.5	119.6
64/80	127.9	126.9
200/80	119.2	114.1
400/80	103.5	100.5

* There are two Θ_{33} for this case.

The computed and measured patterns for the degree of linear polarization $-P_{12}/P_{11}$ are shown in Fig. 5. The upper diagram shows the computed values for a number of aspect ratios and the measured data presented by Dugin and Mirumyants (1976). The computed linear polarization for $L/2a = 0.1$ and 0.2 agrees well with the measured values. In the lower diagram, we compare the computed linear polarization with the measured data presented by Stahl et al. (1983) and Tomasko (personal communication). The experiments used a He–Ne (6328 Å) laser and 15 detectors spaced at 10° increments. The circles shown in Fig. 5b represent the linear polarization values for laboratory columns with a mean length of about 11 μm. Aspect ratios of 2.5 and 5 were used in the scattering calculations to interpret the observations. The computed values for the aspect ratio of 5 closely match the observed linear polarization pattern for columns.

The linear polarization pattern presented in Fig. 5a and b shows that polarization becomes zero (neutral point) at phase angles (180°-scattering angles) between 10° and 30°. For ice columns ($L/2a = 2.5, 5$) or ice crystals with $L \approx 2a$, the neutral point is 17°–19°, but it is 23°–24° for ice plates ($L/2a = 0.1, 0.2, 0.4$). As demonstrated in Part II (Takano and Liou 1988), the location of the neutral point is not affected by multiple scattering. Thus, an observation of the neutral point for clouds may provide a means for determining the shape (column or plate) of cloud particles.

4. Light scattering by horizontally oriented plate and columnar crystals: Interpretation of observed optical phenomena from cirrus

In this section, we present light scattering results for horizontally oriented ice crystals with the specific purpose of interpreting numerous optical features that have been observed in the presence of cirrus. The theory and computation of solar radiative transfer in cirrus

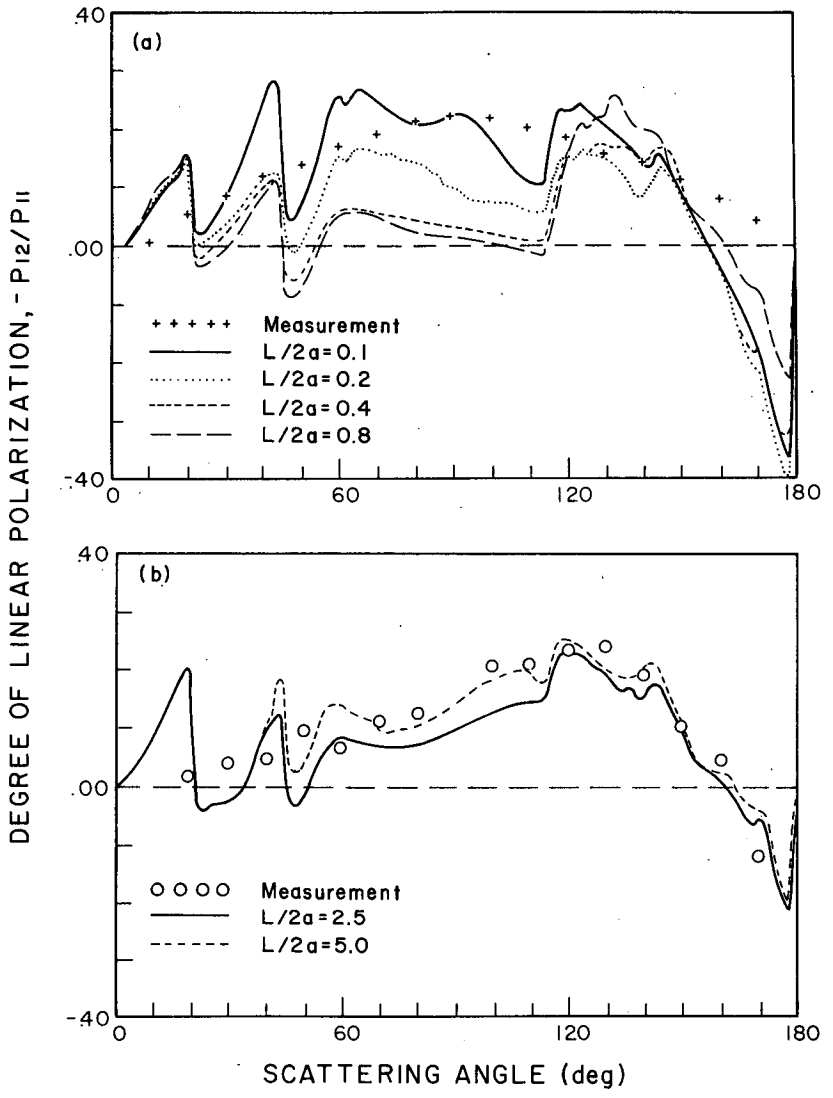

FIG. 5. Degree of linear polarization for randomly oriented ice crystals at $\lambda = 0.55\ \mu$m (a) for plate crystals, and (b) for columnar crystals. The plus and zero symbols are the experimental values reported by Dugin and Mirumyants (1976) and Stahl et al. (1983), respectively.

clouds composed of horizontally oriented ice crystals will be presented in Part II.

We shall begin our discussion with the manner in which the phase functions for horizontally oriented plates and columns were computed. When plate crystals are randomly oriented with their c axes vertical (referred to as 2-D plates), the phase matrix elements P_{kl} are obtained by integrating G_{kl} over the angle β as follows:

$$P_{kl}(\theta_0, \theta, \phi - \phi_0) = \frac{3}{\pi}\int_0^{\pi/3} G_{kl}(\theta_0, \theta, \phi - \phi_0; \beta)d\beta, \quad k, l = 1\text{–}4. \quad (14)$$

As shown in Fig. 6a, β is the angle denoting the rotation of the plate crystal around the c axis and θ_0 is the solar zenith angle, which is the complimentary angle of the solar elevation angle, ϵ. In the case of 2-D plates, ϵ equals α. The scattering angle Θ and the azimuth angle Φ, whose reference plane is XOZ, are calculated by the ray-tracing method (see Cai and Liou 1982). Then, from the scattering geometry in Fig. 6a, θ and $\phi - \phi_0$ in Eq. (14) can be easily computed (see, e.g., Asano 1983). An angular interval $\Delta\beta = 0.5°$ is sufficient to converge the computations for the phase function.

When column crystals have both their c axes and a pair of prism faces horizontal (referred to as Parry columns), the phase matrix elements P_{kl} are expressed by

$$P_{kl}(\theta_0, \theta, \phi - \phi_0) = \frac{3}{\pi^2}\int_{-\pi/2}^{\pi/2} d\gamma \int_0^{\pi/3} G_{kl}(\theta_0, \theta, \phi - \phi_0; \gamma, \beta)\delta(\beta - \beta^*)d\beta, \quad k, l = 1\text{–}4 \quad (15)$$

where $\delta = 1$ when $\beta = \beta^*$ and $\delta = 0$ otherwise. As

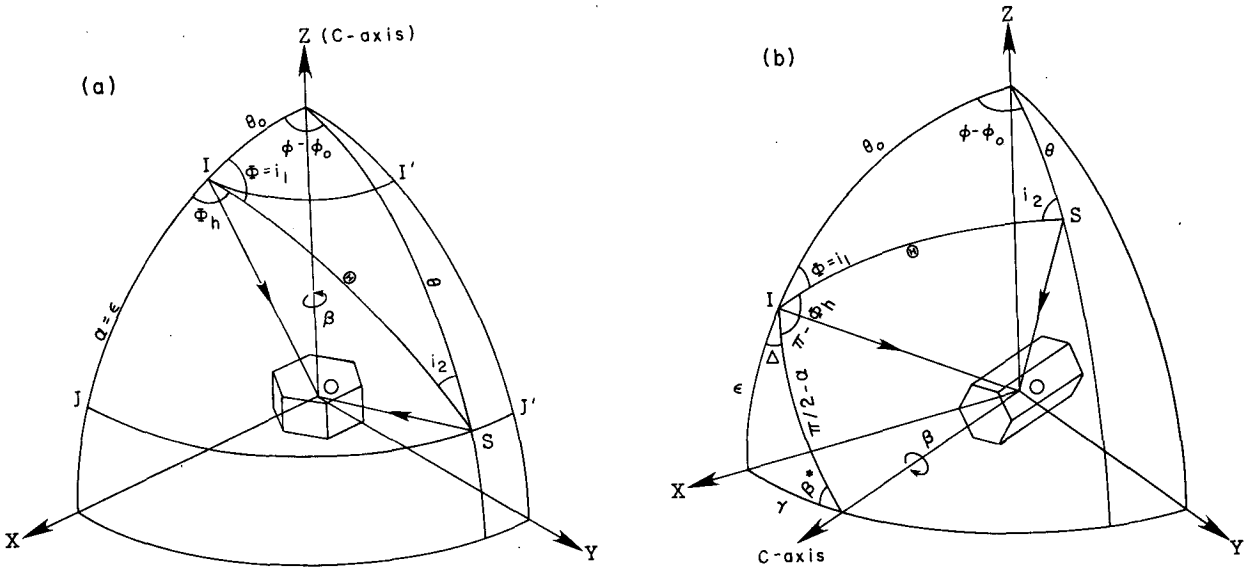

FIG. 6. Scattering geometries for horizontally oriented (a) plate crystals, and (b) columnar crystals. The terms *IO* and *SO* denote the incident and scattered directions, respectively. Other symbols are explained in the text.

shown in Fig. 6b, γ is the angle denoting the orientation of the c axis in the horizontal plane. The angles α and β^* are expressed by

$$\sin\alpha = \cos\epsilon \cos\gamma, \tag{16}$$

$$\sin\beta^* = \sin\epsilon/\sin\alpha. \tag{17}$$

There are two β^* satisfying Eq. (17) in the interval $(0, \pi/3)$. As shown in Fig. 6b, the azimuth angle Φ with respect to the plane XOZ is given by

$$\Phi = \Phi_h - \Delta, \tag{18}$$

where Φ_h is the azimuth angle with respect to the plane containing the c axis of the column and the incident direction IO. The azimuth angle Φ_h is also calculated by the ray-tracing method. The angle Δ is given by

$$\cos\Delta = \frac{\cos\gamma \sin\epsilon}{\cos\alpha}. \tag{19}$$

The set of angles $(\epsilon, \gamma, \Theta, \Phi)$ may be transformed to another set of angles $(\theta_0, \theta, \phi - \phi_0)$, as in the case of 2-D plates. In the numerical computations, we use angular intervals $\Delta\beta = 0.5°$ and $\Delta\gamma = 1°$, which are found to be adequate to obtain stable solutions.

In the case when column crystals orient with their c axes horizontal, as well as with random rotational orientation about the c axes (referred to as 2-D columns), the phase matrix elements P_{kl} may be computed from

$$P_{kl}(\theta_0, \theta, \phi - \phi_0) = \frac{3}{\pi^2}\int_{-\pi/2}^{\pi/2} d\gamma \int_0^{\pi/3} G_{kl}(\theta_0, \theta, \phi - \phi_0; \gamma, \beta)d\beta, \quad k, l = 1\text{–}4. \tag{20}$$

The procedure for computing Eq. (20) is similar to that for Eq. (15).

For interpretation of the optical features produced by cirrus clouds, it is sufficient to use the results from ray tracing involving reflections and refractions. In the following figures, relative scattered intensity rather than absolute intensity due to single scattering will be used for the identification of various halos and arcs. The abbreviations are defined in Table 5.

Figure 7a–c shows the relative intensity as a function of the azimuthal angle $\phi - \phi_0$ for plate crystals with an aspect ratio of 0.1 randomly oriented in the horizontal plane XOY. The solar zenith angles θ_0 ($\pi/2$-elevation angle ϵ) used in the computation are 75°, 50° and 25°. Due to geometry, the scattered light for horizontally oriented plate crystals is confined to four latitude belts denoted by II' and JJ' and their mirror images with respect to the horizontal plane (XOY).

Based on the ray-tracing geometry for plates, the emergent zenith angle θ may be computed from the incoming solar zenith angle θ_0 in the forms

$$\theta^* = \begin{cases} \pi/2 - \sin^{-1}\sqrt{m_r^2 - \sin^2\theta_0} \\ \quad \text{for} \quad \theta_0 > \sin^{-1}\sqrt{m_r^2 - 1} \approx 58° \\ \sin^{-1}\sqrt{m_r^2 - \cos^2\theta_0} \\ \quad \text{for } \theta_0 < \cos^{-1}\sqrt{m_r^2 - 1} \approx 32° \end{cases}. \tag{21}$$

The two latitude belts are associated with $\theta_0(II')$ and its mirror image, $-\theta_0$, while the other two are associated with $\theta^*(JJ')$ and its mirror image, $-\theta^*$. The former two belts define the parhelic and subparhelic circles and the latter two belts are associated with the circumzenithal and subcircumzenithal arcs identified in Fig. 7a.

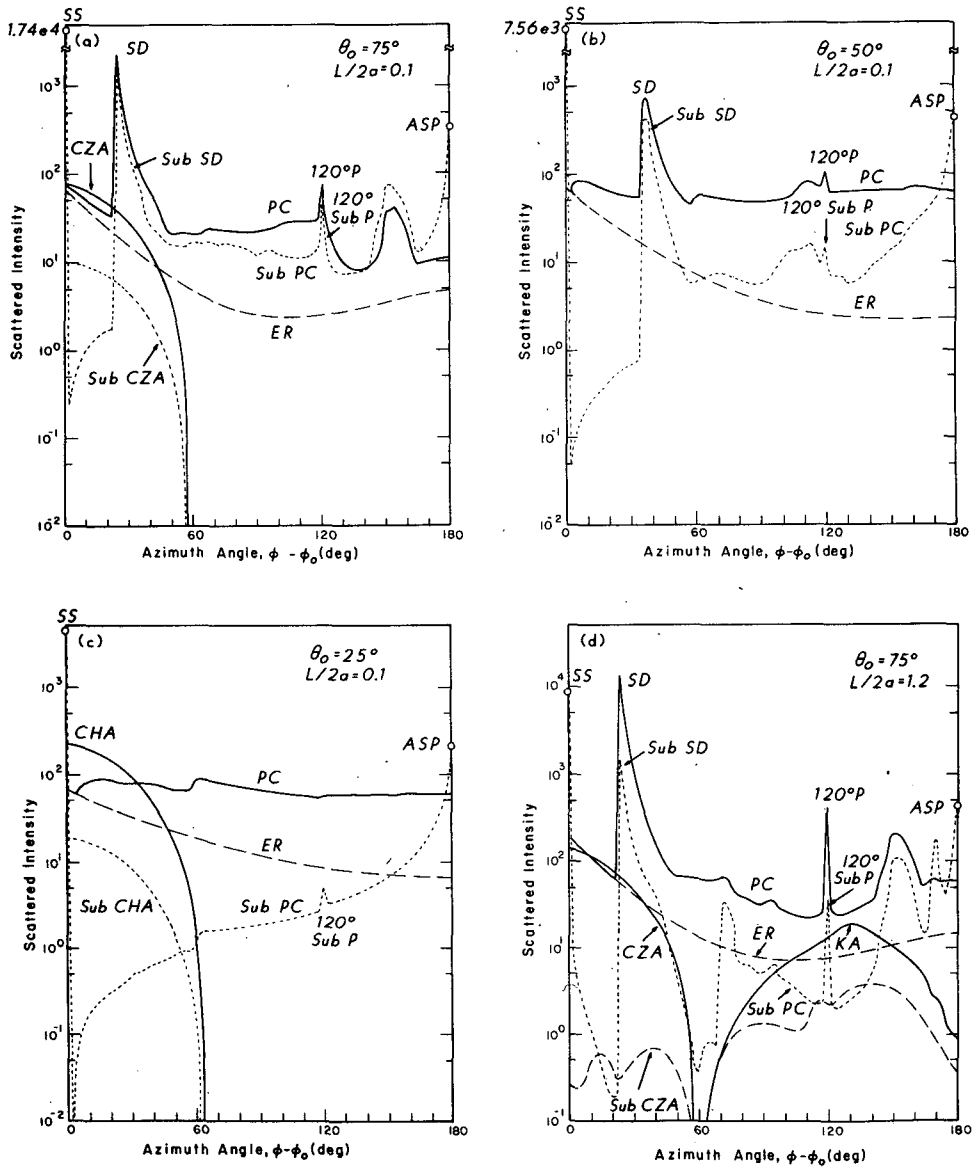

FIG. 7. Scattered intensities for 2-D plates with $L/2a = 0.1$ for (a) $\theta_0 = 75°$, (b) $\theta_0 = 50°$, (c) $\theta_0 = 25°$, and (d) with $L/2a = 1.2$ for $\theta_0 = 75°$ at $\lambda = 0.55$ μm. The abbreviations for the optical features shown in the figure are given in Table 5.

In Fig. 7, the scattered intensity due to external reflection (ER) is plotted for comparison with that produced by various arcs and halos. It is clear that the parhelic circle is a result of light rays undergoing refractions and internal reflections. The intensity pattern of the parhelic circle shows a discontinuity at the azimuthal angle $(\phi - \phi_0)$ of about 122°. This reduction in intensity results from the absence of total reflection for the internally reflected rays. From ray-tracing geometry, the critical angle $(\phi - \phi_0)$ for the total reflection is given by

$$(\phi - \phi_0)_c = 2 \sin^{-1}(\sqrt{m_r^2 - 1}/\sin\theta_0). \quad (22)$$

This formula is also applicable to the parhelic circles produced by horizontally oriented columns. For $\theta_0 = 75°$, we find $(\phi - \phi_0)_c = 122.3°$. The parhelic circle generated in Fig. 7a closely resembles the photograph taken by Evans and Tricker (1972, Fig. 2) for a solar zenith angle θ_0 of about 76°. Several specific features are also identified in this figure and listed in Table 5.

In reference to Eq. (21), when $32° < \theta_0 < 58°$, the scattered light is confined only to the two latitude belts corresponding to $\theta_0(II')$ and its mirror image, $-\theta_0$. If the sun's position is located in this angular range, only the parhelic and subparhelic circles will be produced, as shown in Fig. 7b, which also identifies a number of optical features listed in Table 5.

For a higher sun with a solar zenith angle of 25°,

TABLE 5. Optical phenomena caused by 2-D plates, Parry columns, and 2-D columns.

Abbreviation	Definition
	2-D Plates
ASP	antisolar peak
CHA	circumhorizontal arc
CZA	circumzenithal arc
ER	external reflection
KA	Kern's arc
120°P	120° parhelion
120° Sub-P	120° subparhelion
PC	parhelic circle
SD	sundog (22° parhelion)
SS	subsun
Sub-CHA	subcircumhorizontal arc
Sub-CZA	subcircumzenithal arc
Sub-SD	subsundog (22° subparhelion)
	Parry Columns
ASA	antisolar arc
ASP	antisolar peak
CZA	circumzenithal arc
HA	heliac arc
HAA	Hastings' anthelic arc
LSCP	lower suncave Parry arc
LSVP	lower sunvex Parry arc
SHA	subhelic arc
SID	solar incident direction
SS	subsun
Sub-CZA	subcircumzenithal arc
Sub-PC	subparhelic circle
USCP	upper suncave Parry arc
USVP	upper sunvex Parry arc
	2-D Columns
ASA	antisolar arc
ASP	antisolar peak
DA	diffuse arc
ILA	infralateral arc
LTA	lower tangent arc
PC	parhelic circle
SHA	subhelic arc
SID	solar incident direction
SLA	supralateral arc
TAA	Tricker's anthelic arc
UTA	upper tangent arc
WAA	Wegener's anthelic arc

oriented ice plates produce circumhorizontal and subcircumhorizontal arcs instead of circumzenithal and subcircumzenithal arcs. This is shown in Fig. 7c. Using Eq. (21), the zenith angle θ from which these arcs may be observed is 71.1°. Generally, the intensity of the circumhorizontal arc is stronger than that of the circumzenithal arc. We have also used an aspect ratio of 0.4 in the calculation. All the features identified previously are reproduced with stronger scattered intensities.

In addition, an aspect ratio of 1.2 was used in the light scattering calculations, assuming that these crystals behave the same as plates. The results are presented in Fig. 7d for a solar zenith angle of 75°. The halos and arcs produced in this case are very similar to those presented in Fig. 7a with an addition of the Kern's arc identified in the diagram.

Figure 8 shows the scattered intensity for Parry columns with an aspect ratio of 2.5 and a solar zenith angle of 75°. The scattered intensity in the solar principal plane ($\phi - \phi_0 = 0°$ and 180°) is presented as a function of the zenith angle θ. Due to the specific orientation properties of Parry columns, the scattered intensity is confined to certain areas in the sky. Various halos and arcs are identified in Figs. 8a–d. Additional optical features produced by Parry columns are listed in Table 5. All the optical phenomena have been illustrated by Tricker (1979), Greenler (1980), and Tränkle and Greenler (1987). However, it is noted that the present light scattering program produces the intense antisolar peak (subanthelion) shown in Fig. 8c, which has not been quantitatively presented previously. Also, an arc (referred to as CA), which has not yet been observed, is produced below the parhelic circle shown in Fig. 8d.

Finally, Fig. 9 displays the scattered intensity for 2-D columns in the solar principal plane as a function of the zenith angle using the same aspect ratio for columns and solar zenith angle as in Fig. 8. The scattered light from 2-D columns covers almost the entire sky in contrast to the case of Parry columns. Several halos and arcs produced by 2-D columns are identified in Figs. 9a–d. Additional optical features that can be observed in regions other than the solar principal plane are listed in Table 5. It is noted that the subsun at $\theta = 75°$ cannot be identified definitely due to the overlapping intense lower tangent arc (LTA), as shown in Fig. 9a. The single-scattering patterns shown in Figs. 7–9 will be used for interpretation of the multiple scattering features presented in Part II.

5. Conclusions

A light scattering and polarization program has been developed for computations of the single-scattering properties of cirrus clouds containing hexagonal ice crystals. We have improved our previous ray-tracing program through the incorporation of the birefringence of ice and a proper treatment of the δ-transmission by geometric rays in the 0° scattering angle.

For the first time, the ice crystal size distribution consisting of nonspherical particles is accounted for in the light scattering computations. Four observed distributions for cirrus clouds are employed in the computations. We present the phase function, single-scattering albedo, extinction cross section, and asymmetry factor for wavelengths in the solar spectrum. We also derive a generalized equation for the single-scattering albedo as a function of the absorption parameter $k_i a$, where $k_i = 4\pi(m_i/\lambda)$, m_i is the imaginary part of the refractive index, a the radius of the ice crystal, and λ the incident wavelength. Since the phase function does not vary significantly with wavelength, the parameterized single-scattering albedo equation should be extremely useful for flux and heating rate calculations.

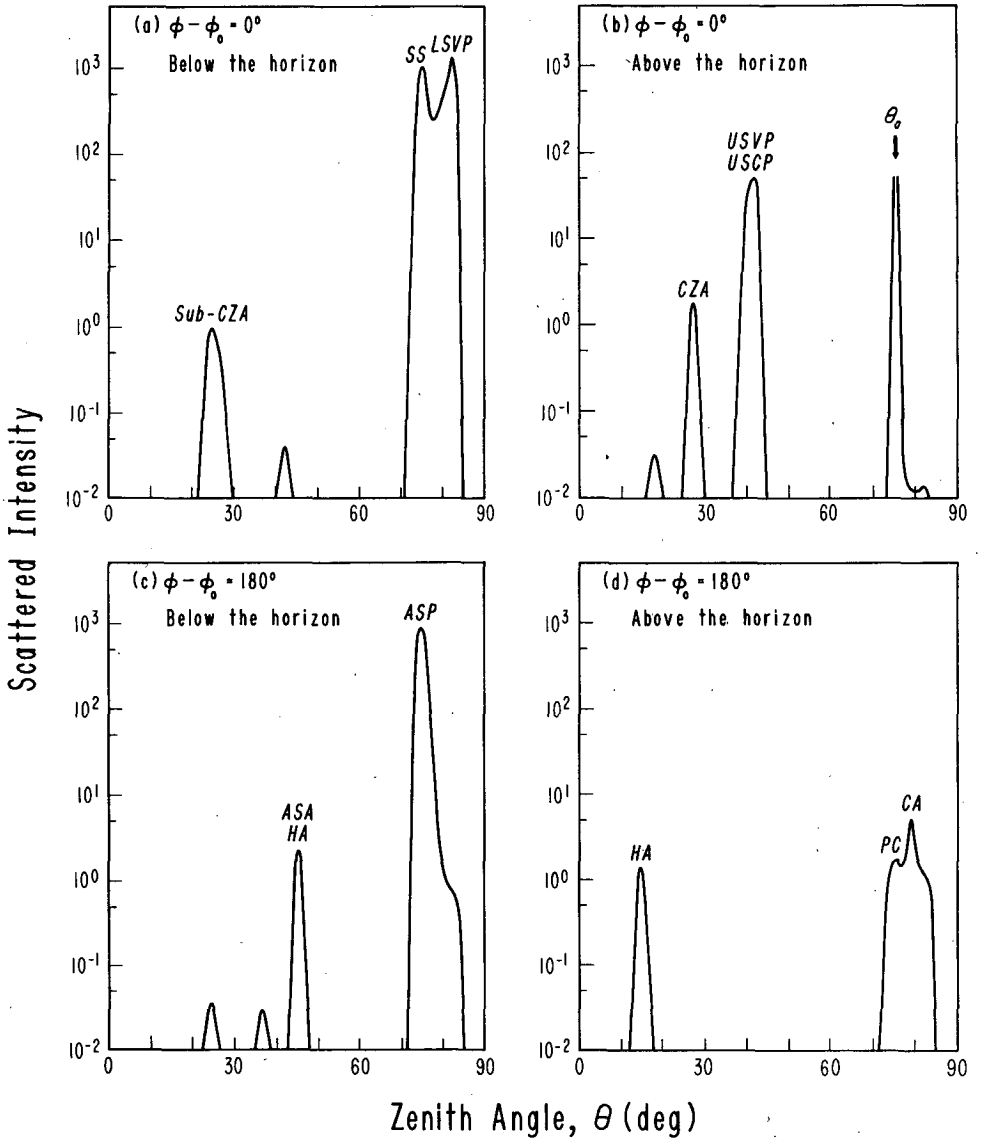

FIG. 8. Scattered intensities in the solar principal plane as functions of the zenith angle θ for Parry columns with $L/2a = 2.5$ for $\theta_0 = 75°$. (a) $\phi - \phi_0 = 0°$ below the horizon, (b) $\phi - \phi_0 = 0°$ above the horizon, (c) $\phi - \phi_0 = 180°$ below the horizon, and (d) $\phi - \phi_0 = 180°$ above the horizon. The abbreviations for the optical features depicted in the figure are given in Table 5.

We also examine the effect of nonsphericity on the single-scattering properties of ice crystals. By using two wavelengths of 0.55 (negligible absorption) and 2.2 μm (moderate absorption) and a number of aspect ratios for hexagonal ice particles, we show that the equivalent sphere with the same surface area or volume as the hexagonal ice crystal is inadequate to reproduce single-scattering properties of hexagonal ice crystals. In general, equivalent ice spheres generate larger asymmetry factors and smaller single-scattering albedos when compared to hexagonal ice particles. This is especially evident for wavelengths at which moderate absorption occurs.

Comparisons with available measurements for light scattering by ice crystals were made using a number of aspect ratios in the ray-tracing calculations. We show that the computed phase matrix elements P_{22}, P_{33}, P_{44}, and P_{43} for plates compare closely with those observed by Dugin and Mirumyants (1976). The effect of birefringence appears to be small, but the incorporation of this effect brings the computed values closer to the observed data. The computed degree of linear polarization patterns agrees well with the observed data presented by Dugin and Mirumyants (1976) and Stahl et al. (1983). We demonstrate that the scattering angle corresponding to zero polarization (neutral point) is

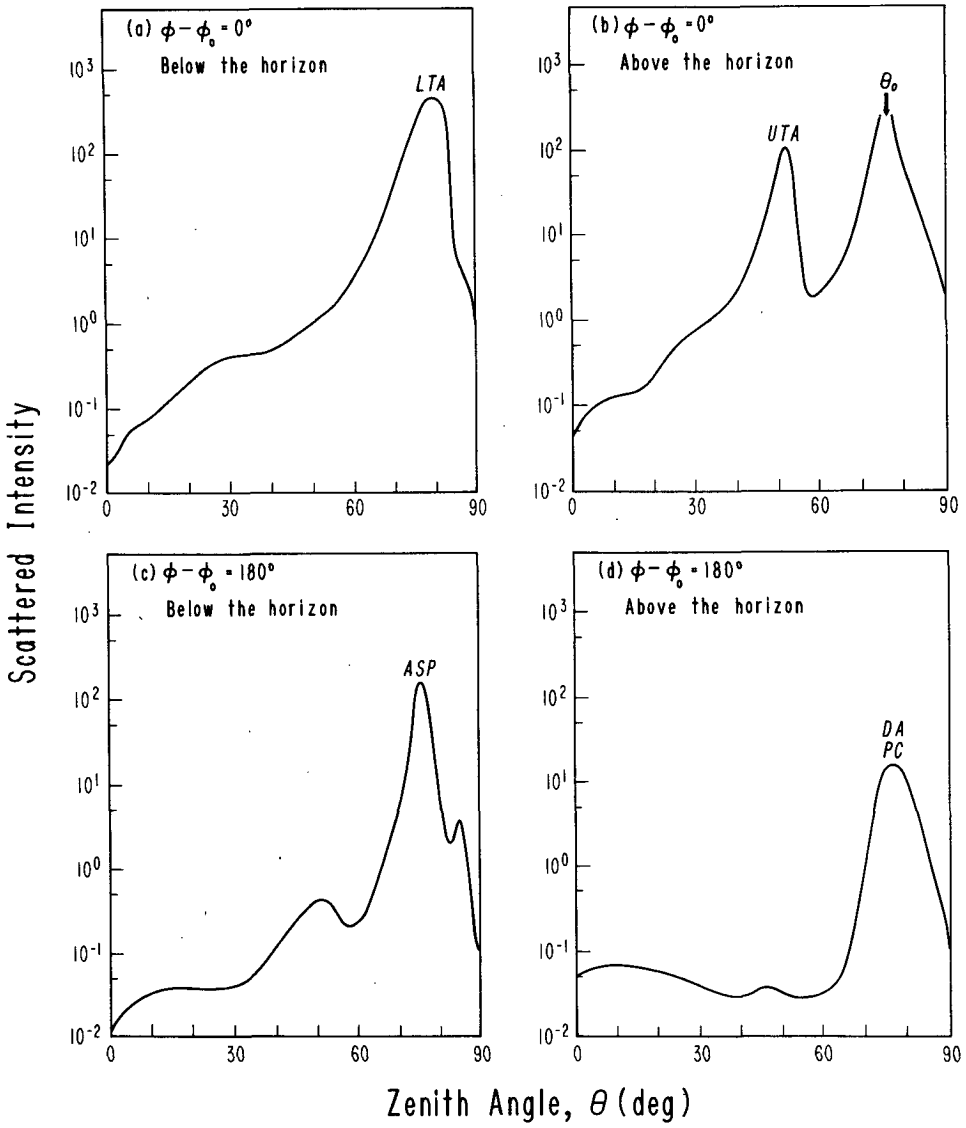

FIG. 9. As in Fig. 8, except for 2-D columns.

extremely sensitive to the aspect ratio of the ice crystal. Finally, to further verify the present light scattering program for hexagonal particles, the computed scattered intensities are used to identify various observed halos and arcs that are produced by horizontally oriented plates and columns. Our calculations are consistent with all the interpretations previously given by the other researchers cited in section 4.

The light scattering program developed in this paper is based on the laws of geometric optics. The computational method is an approximation based on the assumption that light may be thought of as consisting of separate localized rays that travel along straight line paths. It is an asymptotic approach that becomes increasingly accurate as the size parameter (size/wavelength ratio) approaches infinity. In view of the observed ice crystal sizes in cirrus clouds (~20–2000 μm), the ray-tracing method should be valid for solar wavelengths (0.2–3.5 μm). However, for thermal infrared wavelengths (e.g., 10 μm), this method may not be appropriate for small ice crystals. In this case, a separate light scattering program should be developed. Moreover, the present program only deals with hexagonal columns and plates. A modification would be required to account for the scattering by bullet rosettes, which are also frequently observed in cirrus clouds.

Acknowledgments. All the computations contained in this research were carried out on the San Diego supercomputer, CRAY X-MP/48. The research was supported in part by NASA Grant NAG5-732 and NSF Grant ATM85-13975. We thank Graeme Stephens and

the other anonymous reviewer for constructive comments on the paper. Sharon Bennett typed and edited the manuscript.

APPENDIX

Addition of Diffracted and Geometric Optics Rays

When light is scattered by polyhedral particles, such as hexagonal ice crystals, there is δ-function transmission through parallel planes (e.g., a basal plane and opposite basal plane) at $\theta = 0°$. Figure A1 shows a schematic representation of the phase function for this component, along with diffraction and geometric reflection and refraction. The delta forward peak does not contribute to the normalization of the scattering phase function. If the diffracted light rays and geometric optics rays are superimposed conventionally, the normalization integral for the phase function becomes $1 - f_\delta$ where f_δ is the ratio of the δ function at $\theta = 0°$ to the entire scattered light. As shown in Table A1, f_δ becomes larger with increasing $L/2a$ due to a higher probability of plane parallel transmission. It becomes smaller as the wavelength increases due to stronger absorption.

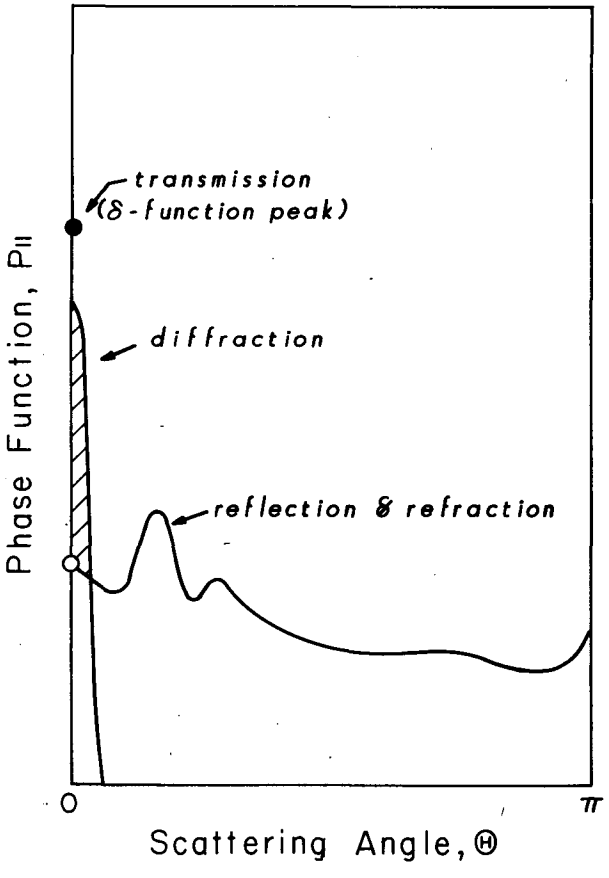

FIG. A1. A schematic representation of the components of the phase function, P_{11} for randomly oriented ice crystals.

TABLE A1. Fraction of the δ-forward transmission ($\theta = 0°$), f_δ.

$L/2a$ (μm/μm)	λ (μm)				
	0.55	1.0	1.6	2.2	3.0
20/20	.12092	.11940	.11563	.10801	5.5296 −6
50/40	.12211	.12053	.11469	.10362	1.1296 −4
120/60	.14062	.13800	.12889	.11181	1.1024 −4
300/100	.15496	.15335	.13783	.11066	1.0831 −4
750/160	.16550	.16364	.13894	.09896	1.0670 −4

Let f_D be the ratio of the diffracted light to the entire scattered light; then the scattering phase matrix may be expressed by

$$G_{kl} = (1 - f_D) \sum_n G_{kl}^{(n)} + \delta_{kl} f_D G_D, \qquad k, l = 1\text{–}4. \tag{A1}$$

Here, $\sum G_{kl}^{(n)}$ and G_D are scattering contributions from rays due to geometric optics and the Fraunhofer diffraction, respectively. Both $\sum G_{kl}^{(n)}$ and G_D are normalized to 1; δ_{kl} is 1 when $k = l$, and 0 otherwise.

In the case of polyhedral particles, f_D may be obtained by the following procedure. Since the extinction cross section C_e is twice the geometric cross section area, the extinction (scattering) cross section for the diffracted light is $C_e/2$. In general, light scattered at $\theta = 0°$ can be regarded as not being scattered at all (van de Hulst 1980). Thus, the cross section of light scattered substantially other than at $\theta = 0°$ is expressed by $C_s(1 - f_\delta)$. It follows that

$$f_D = \frac{1}{2\tilde{\omega}(1 - f_\delta)} \geqslant \frac{1}{2}, \tag{A2}$$

where the single-scattering albedo $\tilde{\omega} = C_s/C_e$. In the case of spherical particles, $f_\delta = 0$. If there is no absorption, $\tilde{\omega} = 1$, and if $f_\delta = 0$, $f_D = ½$.

REFERENCES

Asano, S., 1983: Transfer of solar radiation in optically anisotropic ice clouds. *J. Meteor. Soc. Japan*, **61**, 402–413.

——, and M. Sato, 1980: Light scattering by randomly oriented spheroidal particles. *Appl. Opt.*, **19**, 962–974.

Auer, A. H., Jr., and D. L. Veal, 1970: The dimension of ice crystals in natural clouds. *J. Atmos. Sci.*, **27**, 919–926.

Bohren, C. F., 1986: Absorption and scattering of light by nonspherical particles. *Proc., Sixth Conf. on Atmospheric Radiation*, Amer. Meteor. Soc., 1–7.

Born, M., and E. Wolf, 1975: *Principles of Optics*. Pergamon Press, 808 pp.

Cai, Q., and K. N. Liou, 1982: Polarized light scattering by hexagonal ice crystals: Theory. *Appl. Opt.*, **21**, 3569–3580.

Dugin, V. P., and S. O. Mirumyants, 1976: The light scattering matrices of artificial crystalline clouds. *Izv. Acad. Sci. USSR Atmos. Ocean Phys.*, **12**, 988–991.

Evans, W. F. J., and R. A. R. Tricker, 1972: Unusual arcs in the Saskatoon halo display. *Weather*, **27**, 234–238.

Fraser, A. B., 1979: What size of ice crystals causes the halos? *J. Opt. Soc. Am.*, **69**, 1112–1118.

Greenler, R. G., 1980: *Rainbows, Halos, and Glories.* Cambridge University Press, 195 pp.

Heymsfield, A. J., 1975: Cirrus uncinus generating cells and the evolution of cirriform clouds. *J. Atmos. Sci.*, **32**, 799–808.

——, and C. M. R. Platt, 1984: A parameterization of the particle size spectrum of ice clouds in terms of the ambient temperature and the ice water content. *J. Atmos. Sci.*, **41**, 846–855.

Können, G. P., 1983: Polarization and intensity distributions of refraction halos. *J. Opt. Soc. Am.*, **73**, 1629–1640.

Liou, K. N., 1972: Light scattering by ice clouds in the visible and infrared: A theoretical study. *J. Atmos. Sci.*, **29**, 524–536.

——, 1986: Influence of cirrus clouds on weather and climate processes: A global perspective. *Mon. Wea. Rev.*, **114**, 1167–1199.

Ono, A., 1969: The shape and riming properties of ice crystals in natural clouds. *J. Atmos. Sci.*, **26**, 138–147.

Plass, G. N., and G. W. Kattawar, 1968: Radiative transfer in water and ice clouds in the visible and infrared region. *Appl. Opt.*, **10**, 738–749.

Stahl, H. P., M. G. Tomasko, W. L. Wolfe, N. D. Castillo and K. A. Stahl, 1983: Measurements of the light scattering properties of water ice crystals. Topical Meetings, Meteorological Optics, Optical Society of America, Lake Tahoe.

Starr, D. O., 1987: A cirrus cloud experiment: Intensive field observations planned for FIRE. *Bull. Amer. Meteor. Soc.*, **68**, 119–124.

Stephens, G. L., 1980: Radiative properties of cirrus clouds in the infrared region. *J. Atmos. Sci.*, **37**, 435–446.

Takano, Y., and K. Jayaweera, 1985: Scattering phase matrix for hexagonal ice crystals computed from ray optics. *Appl. Opt.*, **24**, 3254–3263.

——, and K. N. Liou, 1988: Solar radiative transfer in cirrus clouds, Part II: Theory and computation of multiple scattering in an anisotropic medium. *J. Atmos. Sci.* **45**, 20–36.

Thekaekara, M. P., 1973: Solar energy outside the earth's atmosphere. *Solar Energy*, **14**, 109–127.

Tränkle, E., and R. G. Greenler, 1987: Multiple-scattering effects in halo phenomena. *J. Opt. Soc. Am.* **A4**, 591–599.

Tricker, R. A. R., 1979: *Ice Crystal Halos.* Optical Society of America, 53 pp.

van de Hulst, H. C., 1957: *Light Scattering by Small Particles.* Wiley, 470 pp.

——, 1980: *Multiple Light Scattering.* Academic Press, 739 pp.

Vouk, V., 1948: Projected area of convex bodies. *Nature*, **162**, 330–331.

Warren, S. G., 1984: Optical constants of ice from ultraviolet to the microwave. *Appl. Opt.*, **23**, 1206–1225.

Welch, R. M., S. K. Cox and W. G. Zdundkowski, 1980: Calculations of the variability of ice cloud radiative properties at selected solar wavelengths. *Appl. Opt.*, **19**, 3057–3067.